

The haloes of merger remnants

P. J. McMillan^{1,2,3*}, E. Athanassoula² and W. Dehnen¹

¹Department of Physics & Astronomy, University of Leicester, Leicester, LE1 7RH, UK

²LAM, Observatoire Astronomique de Marseille Provence, 2 Place Le Verrier, F-13248 Marseille Cedex 4, France

³Rudolf Peierls Centre for Theoretical Physics, 1 Keble Road, Oxford, OX1 3NP, UK

17 December 2018

ABSTRACT

We perform collisionless N -body simulations of 1:1 galaxy mergers, using models which include a galaxy halo, disc and bulge, focusing on the behaviour of the halo component. The galaxy models are constructed without recourse to a Maxwellian approximation. We investigate the effect of varying the galaxies' orientation, their mutual orbit, and the initial velocity anisotropy or cusp strength of the haloes upon the remnant halo density profiles and shape, as well as on the kinematics. We observe that the halo density profile (determined as a spherical average, an approximation we find appropriate) is exceptionally robust in mergers, and that the velocity anisotropy of our remnant haloes is nearly independent of the orbits or initial anisotropy of the haloes. The remnants follow the halo anisotropy - local density slope ($\beta - \gamma$) relation suggested by Hansen & Moore (2006) in the inner parts of the halo, but β is systematically lower than this relation predicts in the outer parts. Remnant halo axis ratios are strongly dependent on the initial parameters of the haloes and on their orbits. We also find that the remnant haloes are significantly less spherical than those described in studies of simulations which include gas cooling.

Key words: Methods: N -body simulations – Galaxies: kinematics and dynamics – Galaxies: interactions – Galaxies: haloes

1 INTRODUCTION

Simulations of structure formation in the Λ CDM cosmology paradigm consistently produce triaxial dark matter haloes with density profiles with $\rho \rightarrow \infty$ as $r \rightarrow 0$. This is commonly referred to as a density “cusp”. In particular, it is found that the spherically-averaged density profile in the inner halo follows a power law, $\rho \propto r^{-\gamma_0}$ with $\gamma_0 \sim 1$, while in the outer parts of the halo $\rho \propto r^{-3}$ (e.g. Navarro et al. 1996; Moore et al. 1998; Power et al. 2003). This applies universally over all mass ranges investigated.

The asphericity of dark matter haloes is also a generic prediction of Λ CDM simulations (e.g. Dubinski & Carlberg 1991; Allgood et al. 2006), with typical minor-to-major axes ratios $c/a \sim 0.6–0.7$ for a Milky Way sized galaxy. However, observations of the tidal stream of the Sagittarius dwarf spheroidal have been used to argue that the halo of the Milky Way is nearly spherical, with $c/a < 0.7$ ruled out to a high degree of confidence for Galactocentric distances in the range $16\text{kpc} < r < 60\text{kpc}$ (Ibata et al. 2001; Majewski et al. 2003). This is not necessarily a surprising result, since simulations which take into account the effect of gas cooling on dark matter haloes find that it results in haloes that are sig-

nificantly more spherical than those found in pure CDM simulations (e.g. Katz & Gunn 1991; Kazantzidis et al. 2004).

Hansen & Moore (2006) found that there is also an apparently universal relationship between the local density slope and velocity anisotropy of simulated dark matter haloes. They argued that this could be understood through a recognition that the density slope in the tangential direction was zero (for a spherical halo), and that the shape of a velocity distribution is directly dependent on the density slope (which is known for simple structures; e.g. Hansen et al. 2005). The anisotropy of the halo is parameterised by

$$\beta \equiv 1 - \frac{\sigma_\theta^2 + \sigma_\phi^2}{2\sigma_r^2}, \quad (1)$$

and the local density slope as

$$\gamma(r) = -\frac{d \log \rho(r)}{d \log(r)}. \quad (2)$$

Hansen & Moore suggested that the anisotropy relates to the density slope as

$$\beta(\gamma) = 1 - \xi(1 - \gamma/6). \quad (3)$$

They used data from collapse, merger and cosmological simulations to support their hypothesis, and found that the best fit to their data come from taking the free parameter $\xi \simeq 1.15$. Dehnen & McLaughlin (2005) showed that as

* E-mail: p.mcmillan1@physics.ox.ac.uk

suming this relationship, spherical symmetry, and the relationship $\rho/\sigma_r^3 \propto r^{-\alpha}$ where α is some constant (e.g. Taylor & Navarro 2001), defines a single analytical dynamical equilibrium for a dark matter halo, independent of α with a density profile which closely resembles that found in simulations.

Since the work of Toomre & Toomre (1972) on the tidal origin of bridges and tails, it has been recognised that elliptical galaxies could be formed by the merger of two disc galaxies. Various authors have conducted numerical (N -body) simulations of collisionless mergers, some focusing on the stellar disc component (e.g. Negroponte & White 1983; Barnes 1988; Hernquist & Ostriker 1992; Naab & Burkert 2003), some on the dark matter halo (e.g. White 1978; Villumsen 1983; Boylan-Kolchin & Ma 2004; Kazantzidis et al. 2004; Aceves & Velázquez 2006; Kazantzidis et al. 2006).

The studies of White, Villumsen and Boylan-Kolchin & Ma, and most other studies of the halo component used idealised, spherically symmetric systems to represent the galaxies. There are relatively few studies of the remnant haloes of mergers between haloes containing disc galaxies.

Kazantzidis et al. (2004) looked at the shapes of dark matter haloes, primarily considering the effect of gas cooling, but also reporting simulations of collisionless mergers of galaxies with disc components. They stated that the shape of the remnant halo depends sensitively on the relative inclination of the discs. Aceves & Velázquez (2006) conducted simulations of mergers of galaxies with mass-ratios of 1:1, 1:3 and 1:10, determining that in each case the initial ‘‘cusp’’ density profile was preserved. Kazantzidis et al. (2006), as part of a larger study of dark matter halo mergers, included simulations of binary (1:1 mass-ratio) mergers of haloes with disc components. They too found that the presence of a disc did not affect the conclusion that ‘‘dissipationless mergers result in remnants that are practically scaled versions of their progenitors’’.

All three of these papers create their initial conditions using the prescription of Hernquist (1993), which makes the approximation of a locally Maxwellian velocity distribution, with mean velocity and the dispersion tensor found from the moment equations. This method is far from rigorous as the true equilibrium velocity distribution can be strongly non-Maxwellian.

Novak et al. (2006) looked at the shapes of both the stellar and dark matter components of the remnants from SPH simulations of major mergers. They found that the stellar remnants were generally oblate, while the haloes were prolate or triaxial. The initial haloes in their simulations were spherical, and the majority of remnant haloes were still relatively close to spherical, having $c/a > 0.75$, with no haloes from any of the 58 simulations having $c/a < 0.6$.

The most useful observational work on individual dark matter halo shapes for elliptical galaxies, Buote & Canizares (1996, 1998) and Buote et al. (2002), uses measurements of the flattening of X-ray isophotes to place constraints on the ellipticity of the dark matter haloes of elliptical galaxies NGC1332, NGC3923 and NGC720, under the assumption that gas rotation has a negligible effect. They find that all the haloes are substantially flattened, with $0.28 < c/a < 0.65$, and place tight constraints on the ellipticity of NGC720, which has $c/a = 0.38 \pm 0.05$ for any of

their oblate density models, and $c/a = 0.37 \pm 0.04$ for any of their prolate models.

No previous simulation studies give a thorough global overview of the properties of the haloes of merger remnants, covering their structural and kinematic aspects. We perform collisionless N -body simulations of 1:1 mass ratio mergers of galaxy models consisting of bulge, disc and halo components. A new method for creating a self-consistent equilibrium model of these components is introduced, which avoids the use of the local Maxwellian approximation. We examine the effects of the initial galaxy orientation, pericentre separation of the mutual parabolic orbit (which we also refer to as the ‘‘impact parameter’’), initial anisotropy of the galaxy halo, and cusp strength on the density profile, shape, and kinematics of the remnant halo.

In Sections 2.1 and 2.2 we describe the galaxy models used in our simulations; in Section 2.3 the various suites of simulations we perform are detailed; the density profiles, kinematics, and shapes of the remnant haloes are examined in Sections 3.1, 3.2 and 3.3 respectively. Finally we discuss our results and draw conclusions.

2 GALAXY MODELS AND SIMULATIONS

2.1 Initial Conditions

The problem of building an equilibrium disc-bulge-halo system is a long standing issue, addressed in many different ways in the literature (e.g. Hernquist 1993; Widrow & Dubinski 2005). Our approach is new, is described in McMillan (2006), and will be presented in a future paper (McMillan & Dehnen 2007). This approach bears some relation to that of Barnes (1988), in that the non-spherically symmetric component (the disc), is grown adiabatically within the spheroid. The process has three stages:

(i) Creating an equilibrium initial N -body representation of the spherically symmetric components of the galaxy (the halo and bulge) in the presence of an applied potential field corresponding to the monopole (spherical average) of the desired disc potential. The distribution function of the halo and bulge is that of Cuddeford (1991). This distribution function has

$$\beta(r) = \frac{\beta_0 r^2 + r_a^2}{r^2 + r_a^2}, \quad (4)$$

This allows for constant β (as $r_a \rightarrow \infty$) or for Osipkov-Merritt-model-like anisotropy (with $\beta_0 = 0$) (Osipkov 1979; Merritt 1985).

(ii) Evolving the N -body system whilst growing the non-monopole components of the disc potential adiabatically in simulation, allowing halo and bulge particles time to relax into the full potential of the disc.

(iii) Populating the disc component with particles. We use an implementation of the disc distribution function f_{new} defined in Dehnen (1999), see Equation 7 of this paper.

For the halo we use a spherically-symmetric truncated generalised Navarro et al. (1996, NFW) like profile:

$$\rho_h(r) = \frac{\rho_c}{(r/r_h)^{\gamma_0} (1 + r/r_h)^{3-\gamma_0}} \text{sech}(r/r_t), \quad (5)$$

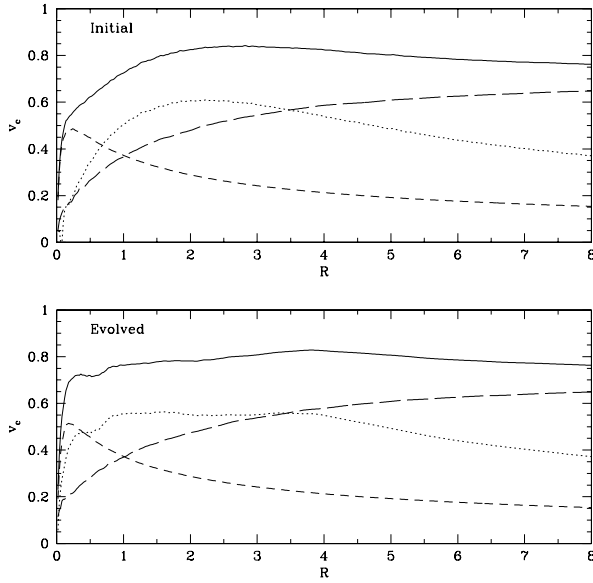


Figure 1. Rotation curve in the plane of the disc for our standard $\gamma_0 = 1$ galaxy model, shown for both the initial conditions (*upper*), and after being allowed to evolve in isolation for 300 time units (approximately the time it takes the galaxies to reach pericentre in our merger simulations – *lower*) The solid line is the net rotation curve, also shown are the decomposed contributions from the disc (*dotted*), bulge (*short-dashed*), and halo (*long-dashed*). The evolution seen is dominated by that in the inner $\sim 2R_d$ of the disc component. This is caused by a bar instability in the disc which redistributes its mass. This, in turn, has some effect on the halo at its innermost radii (see Section 2.3).

where ρ_c is a scale density, r_h is the halo scale radius, r_t is the halo truncation radius, and γ_0 describes the inner slope of the density profile. As $r \rightarrow 0$, the halo density $\rho_h \propto r^{-\gamma_0}$. We truncate at a radius significantly larger than the halo scale radius, so in the outer halo the density goes as $\rho_h \propto r^{-3} \operatorname{sech}(r/r_t)$. Some truncation is necessary as the untruncated profile ($r_t \rightarrow \infty$) is infinitely massive.

The disc is defined as having a surface density profile which is exponential in the cylindrical radius R , and a vertical (z -component) structure modelled by isothermal sheets

$$\rho_d(R, z) = \frac{M_d}{4\pi R_d^2 z_d} \exp\left(-\frac{R}{R_d}\right) \operatorname{sech}^2\left(\frac{z}{z_d}\right), \quad (6)$$

where M_d is the total disc mass, R_d is the disc scale radius, and z_d the scale height.

To find the distribution function of the disc, we assume that it can be decomposed into its components in the plane of the disc, and perpendicular to it, i.e. $f_d \cong f_d(E_p, L_z, E_z)$ where the “vertical(z -component) energy” $E_z \equiv \frac{1}{2}v_z^2 + \Phi(R, z) - \Phi(R, 0)$, and the “planar energy” $E_p = E - E_z = \frac{1}{2}(v_R^2 + v_\theta^2) + \Phi(R, 0)$.

If we define R_{EP} as the radius of a circular orbit in the disc midplane with planar energy E_p , we can write the

planer component of the disc distribution function as

$$f_{d,p}(E_p, L_z) = \frac{\Omega(R_{EP}) \Sigma'(R_{EP})}{\pi \kappa(R_{EP}) \sigma_R'^2(R_{EP})} \exp\left[\frac{\Omega(R_{EP})[L_z - L_{z,c}(E_p)]}{\sigma_R'^2(R_{EP})}\right], \quad (7)$$

where $L_{z,c}(E)$ is the angular momentum of a circular orbit in the disc midplane with planar energy E_p , Ω is the circular frequency of that orbit, and κ is the epicycle frequency. $\Sigma'(R)$ and $\sigma_R'^2(R)$ are defined such that the true surface density $\Sigma(R)$ and radial velocity dispersion $\sigma_R^2(R)$ of the N -body representation are those desired, to within an appropriate degree of accuracy.

We model the bulge as non-rotating, initially spherically symmetric and with a Hernquist (1990) density profile.

$$\rho_b(r) = \frac{M_b}{2\pi} \frac{r_b}{r(r_b + r)^3}, \quad (8)$$

where M_b is the mass of the bulge, and r_b is its scale radius.

We performed a suite of simulations in an effort to investigate the effect of the properties of the progenitors and of the encounter on the halo of the merger of two equal-mass galaxies. The galaxy models were designed to loosely resemble the Milky Way as described by Klypin, Zhao, & Somerville (2002).

2.2 Numerical Miscellanea

In all our models we choose units such that the disc scale length, $R_d = 1$, disc mass $M_d = 1$, and the constant of gravity $G = 1$. The disc scale height was chosen to be $z_d = 0.1$, the velocity dispersion of the disc was defined such that the Toomre (1964) stability parameter $Q = 1.2$ at all radii. The bulge mass $M_b = 0.2$, and bulge scale length $r_b = 0.2$. Scaling these values to the Milky Way, taking $R_d = 3.5\text{kpc}$, $M_d + M_b = 5 \times 10^{10} M_\odot$ gives a time unit $\simeq 14\text{Myr}$. We chose to have the scale radius of the halo $r_h = 6$, the truncation radius $r_t = 60$, and the halo mass $M_h = 24$. In simulations with $\gamma_0 = 1.0$, 79% of this total mass is within the truncation radius. The rotation curve for this model is shown in Figure 1.

The stellar components were populated with 150 000 equal mass particles (i.e. 125 000 in the disc, 25 000 in the bulge) with a smoothing length $\epsilon_{\text{stellar}} = 0.02$. The halo component was populated with 750 000 equal mass particles with a smoothing length $\epsilon_{\text{halo}} = 0.04$. That corresponds to each halo particle being 4 times more massive than a stellar particle. A small number of simulations with 4 times more particles were performed for comparison. These demonstrated that the numerical resolution used was sufficient.

The N -body simulations were performed using the publicly available N -body code *gyrfalCON*, which is based on Dehnen’s (2000; 2002) force solver *falcON*, a tree code with mutual cell-cell interactions and complexity $\mathcal{O}(N)$. The equations of motion were integrated using the familiar leap-frog integrator with minimum time step 2^{-7} and a block-step scheme allowing steps up to eight times larger. Individual particle time steps were adjusted in an (almost) time-symmetric fashion such that on average

$$\tau_i = \min \left\{ \frac{0.01}{|a_i|}, \frac{0.05}{|\Phi_i|} \right\}, \quad (9)$$

with Φ_i and \mathbf{a}_i the gravitational potential and acceleration of the i th body. With these parameters, energy was conserved to within 0.1% over the full time span (1000 time units) in a typical simulation, approximately corresponding to a Hubble time. The time span was chosen such that there is sufficient time for the remnant to reach a dynamical equilibrium.

In all simulations the equal mass galaxies were placed on a mutual orbit in the x-y plane. In the vast majority of cases these orbits were parabolic and corresponded to one that would have a pericentre separation of $8 R_d$ if the galaxies were point masses; we refer to this distance as the “impact parameter” d of the merger. In some cases the galaxies were placed on orbits with smaller pericentre separations, or on a radial orbit with zero net energy (i.e. a parabolic orbit in the limit where impact parameter $d \rightarrow 0$). The galaxy centres were initially separated by $200R_d$.

2.3 Suites of simulations

We perform four suites of simulations of equal-mass mergers, to examine the effects of varying different parameters on the mergers. The suites vary in

- (i) Orientation of the disc galaxy.
- (ii) Pericentre separation of the galaxies’ mutual orbit.
- (iii) Initial velocity anisotropy of the halo component.
- (iv) Cusp strength of the haloes (γ_0 in Equation 5).

In addition, we ran control simulations, which were stand-alone simulations of the same galaxy models, run for the same length of time, with no merger. The galaxy disc is bar-unstable, which in these simulations causes a steepening in the density profile of the inner parts of the disc, which also causes a steepening in the halo profile in the inner $\sim 0.2r_h$. This steepening is commonly observed in simulations of barred galaxy evolution (reviewed e.g. by Athanassoula 2004). The effect of this evolution on the rotation curve of the galaxy can be seen in Figure 1. The anisotropy of the halo velocity distribution is essentially unchanged by the stand-alone evolution.

2.3.1 Suite 1: Orientation

Our first suite of simulations consisted of 16 mergers which vary only in the orientation of the discs with respect to one another, and to the angular momentum vector of their mutual orbit. Following the example of Barnes (1988), we define four different orientations for the spin vector of each galaxy disc, corresponding to pointing towards the four vertices of a regular tetrahedron. The orientations of disc galaxies in mergers are usually described in terms of the disc inclination relative to the orbital plane i , and the argument of pericentre ω (See also Figure 2 or Toomre & Toomre 1972). The inclinations (i_1 & i_2), and arguments of pericentre (ω_1 & ω_2) for the suite of mergers are shown in Table 1.

These are the same initial orientations that were used in the collisionless merger simulations of Naab & Burkert (2003) and the SPH merger simulations of Naab, Jesseit, & Burkert (2006). These studies detailed the significant effects that varying the initial disk orientations has upon the properties of the *luminous* components of the merger remnants.

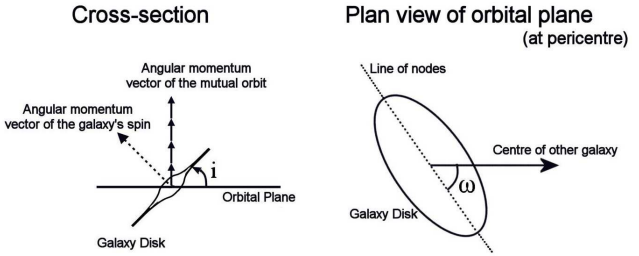


Figure 2. Diagram showing the definitions of inclination i , and argument of pericentre ω for the mergers. By convention, $-180^\circ < i \leq 180^\circ$, $-90^\circ < \omega < 90^\circ$. The “line of nodes” is the intersection of the plane of the galaxy disc with the orbital plane. The cross section view (left) is that from a point in both the plane of the orbit (shown as the horizontal), and the plane of the galaxy disc (shown at an angle i to the horizontal). The plan view is from above the orbital plane, looking down.

In all cases the initial halo has an inner density slope $\gamma_0 = 1.0$ (Equation 5), and an isotropic ($\beta = 0$) velocity distribution. The galaxies were put on a parabolic orbit with a pericentre separation of $8R_d$.

TABLE 1

| # | Disc 1 | | Disc 2 | |
|----|--------|------------|--------|------------|
| | i_1 | ω_1 | i_2 | ω_2 |
| 1 | 0 | 0 | 180 | 0 |
| 2 | 0 | 0 | 71 | 30 |
| 3 | 0 | 0 | 71 | -30 |
| 4 | 0 | 0 | 71 | 90 |
| 5 | -109 | -60 | 180 | 0 |
| 6 | -109 | -60 | 71 | 30 |
| 7 | -109 | -60 | 71 | -30 |
| 8 | -109 | -60 | 71 | 90 |
| 9 | -109 | 0 | 180 | 0 |
| 10 | -109 | 0 | 71 | 30 |
| 11 | -109 | 0 | 71 | -30 |
| 12 | -109 | 0 | 71 | 90 |
| 13 | -109 | 60 | 180 | 0 |
| 14 | -109 | 60 | 71 | 30 |
| 15 | -109 | 60 | 71 | -30 |
| 16 | -109 | 60 | 71 | 90 |

2.3.2 Suite 2: Impact parameter

We performed two sets of simulations with galaxy models identical to those used in Suite 1, varying the separation at pericentre (impact parameter) d between $8R_d$ and 0 (i.e. radial impact) in increments of $2R_d$. The two sets of simulations differ in the galaxy orientations, which correspond to those of simulations 4 & 7 in suite 1 (Table 1).

2.3.3 Suite 3: Halo anisotropy

Our third suite of simulations consisted of mergers of galaxies with varying initial halo velocity dispersions and were performed to examine the effect that has on remnant properties. The haloes had identical density profiles to those

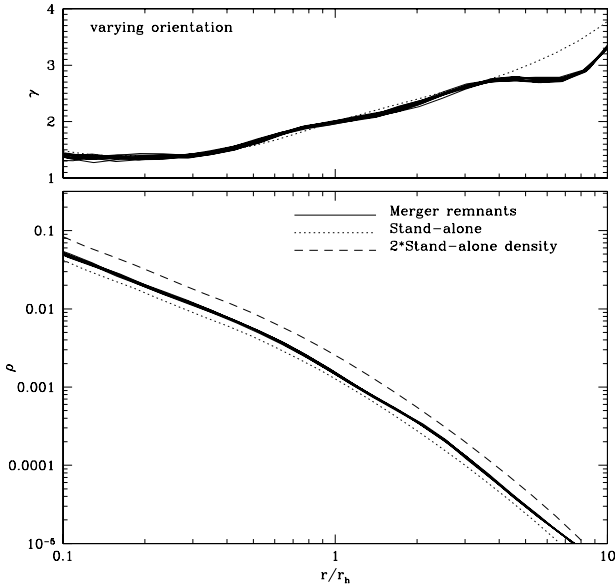


Figure 3. Suite 1: Spherically averaged density profile (*lower*) and density slope profile (γ , see Equation 2; *upper*) for remnant haloes from the 16 simulations in suite 1 (*solid lines*). Also shown, for comparison, is the density profile and slope of the halo of the equivalent stand-alone simulation (*dotted*), and the same stand-alone density profile with the density doubled - i.e. what one would expect if the galaxies were simply stacked on top of one another (*dashed*).

in suites 1 and 2, but rather than an isotropic velocity distribution, they were initialised with constant radial anisotropy ($\beta = 0.35$ throughout the halo), constant tangential anisotropy ($\beta = -0.4$ throughout the halo), or Osipkov-Merritt-model-like anisotropy (Equation 4) with $r_a = 24 = 4r_h$. Simulations were performed with galaxies orientated as per orientation 7 (Table 1), and with impact parameters of 8, 3, and $0R_d$.

2.3.4 Suite 4: Cusp strength

We ran a series of simulations with varying halo cusp strengths. The inner slope of the density distribution (γ_0 in Equation 5) varied between $\gamma_0 = 0.1$ and $\gamma_0 = 1.6$. In all cases we retained the parameters $r_h = 6$, $r_t = 60$ and $M_h = 24$. The galaxy discs had the same orientations as simulation 4 in Table 1. The haloes all had isotropic velocity distributions, and the mergers trajectories all had impact parameter $d = 8R_d$.

3 RESULTS

3.1 Halo density profiles

The haloes of the merger remnants are not spherically symmetrical (see Section 3.3), however insight, and a comparison with previous work, can be found from looking at spherically averaged density profiles, and local density slopes (Equation 2).

Figure 3 shows the density profiles and slopes for the

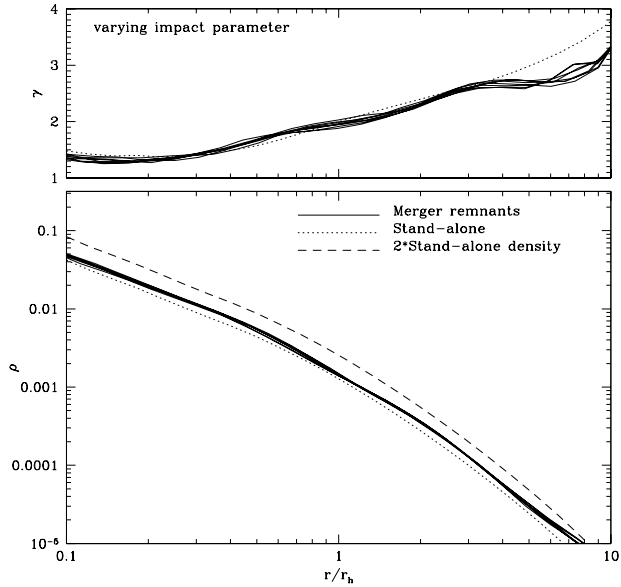


Figure 4. Suite 2: Spherically averaged density profile and density slope profile for remnant haloes, as in Figure 3, for simulations with impact parameters $d = 8, 6, 4, 2, 0R_d$ (*solid lines*).

16 merger remnants from suite 1 (Section 2.3.1), with the equivalent for the stand-alone simulations. The disc orientations have no effect on the density profile, even in the regions where they dominate the galaxies' density. The shape of the remnant density profile is very similar to that of the initial haloes, with an almost identical scale length. There are, however differences in the outer parts: $\sim 6\%$ of the halo mass becomes unbound during the merger, and the mass within $10r_h$ is $\sim 50\%$ of the total mass of the original haloes (as compared to 79% in each halo initially). Hence the density within the inner $\sim 10r_h$ of the merged haloes is closer to that of one of the initial haloes than to double that (as it would be if the merger was equivalent to simply “freezing” the haloes, and placing them on top of one another).

The simulations of suite 2 show that varying the impact parameter of mergers also has little effect on the shape of the density profile (Figure 4). Results for suite 4 showed the same trends for all cusp strengths. In the interests of brevity, only the results for $\gamma_0 = 0.1$ and $\gamma_0 = 1.4$ are shown (Figure 5).

Results from suite 3 do show a slight trend in remnant cusp strength with initial halo anisotropy. The trend is observable for all orbital separations simulated, but only results from simulations with orbital separation $d = 8R_d$ are shown in Figure 6, for clarity. Haloes which have initially constant tangential anisotropy have sharper remnant cusps than initially isotropic haloes, while haloes with initial constant radial anisotropy have weaker remnant cusps. Giving the haloes Osipkov-Merritt anisotropy does not alter the cusp strength. Compared to the isotropic case, cusp strength – measured in terms of $\gamma(r)$ at small radii – is ~ 0.1 greater for the $\beta = 0.35$ case than for the isotropic case, and is ~ 0.1 less in the $\beta = -0.4$ case. This trend is not seen in the stand-alone profiles, which are nearly identical in all three cases.

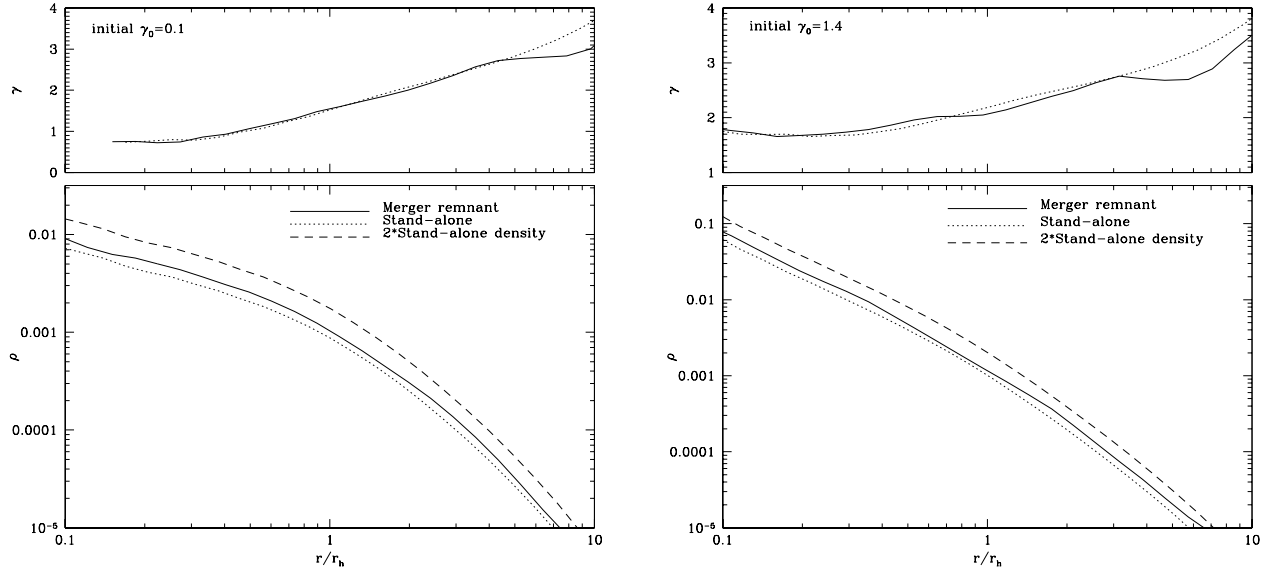


Figure 5. Suite 4: Spherically averaged density profile and density slope profile for stand-alone and remnant haloes, as in Figure 3. The initial haloes had $\gamma_0 = 0.1$ (left) or $\gamma_0 = 1.4$ (right) density cusps.

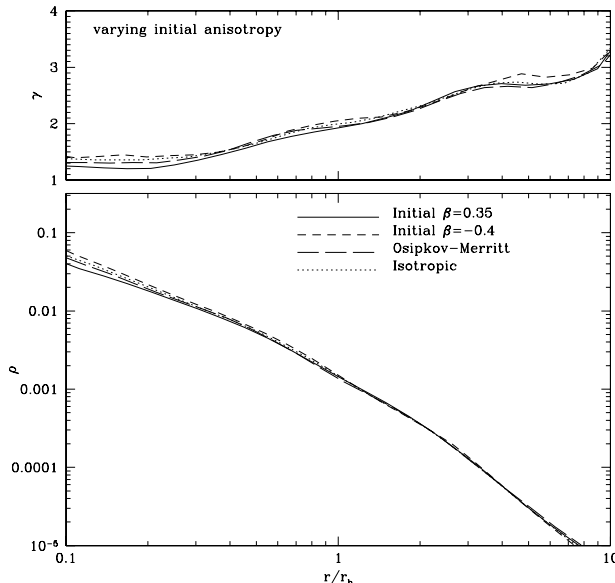


Figure 6. Suite 3: Spherically averaged density profile and density slope profile for remnant haloes from $d = 8R_a$ mergers in which the initial haloes had constant radial anisotropy ($\beta = 0.35$: solid line); constant tangential anisotropy ($\beta = -0.4$: short-dashed); Osipkov-Merritt anisotropy ($r_a = 24$: long-dashed) Also shown are the density profile and slope for the equivalent mergers with initially isotropic haloes, as in all other simulations (dotted).

3.2 Halo velocity distributions

We investigate the velocity distribution of the haloes by looking at β as a function of radius, and as a function of the local density slope $\gamma(r)$. β is determined for particles in

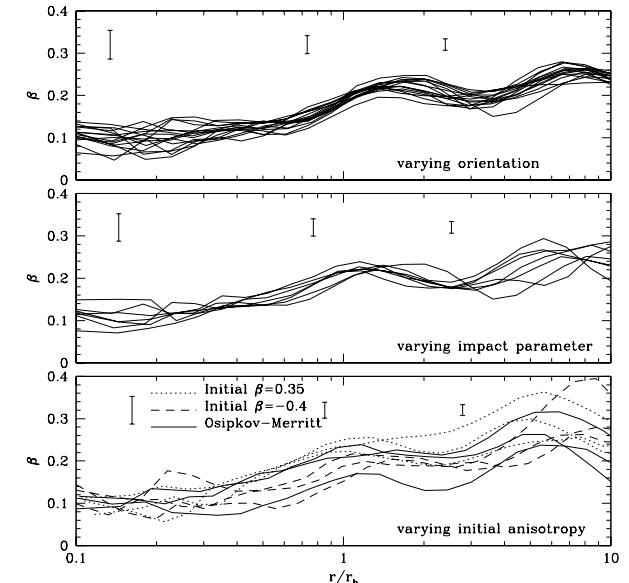


Figure 7. β as a function of radius for the simulations of suites 1-3 (top to bottom). Error bars shown are typical of all simulations in respective plot, found using Equation 10. In the bottom plot remnants of mergers with haloes with different initial anisotropies are represented by different line types. Dotted lines plot β for remnants of initial halo $\beta = 0.35$ mergers, dashed lines for initial halo $\beta = -0.4$, solid lines for the Osipkov-Merritt haloes.

spherical shells, with the median particle radius for the shell being the value plotted in Figures 7 & 8.

Error estimates, as shown in Figures 7 and 8 were found for the spherical shell of particles through the standard propagation of errors formula, such that the error $\Delta\beta$ is given

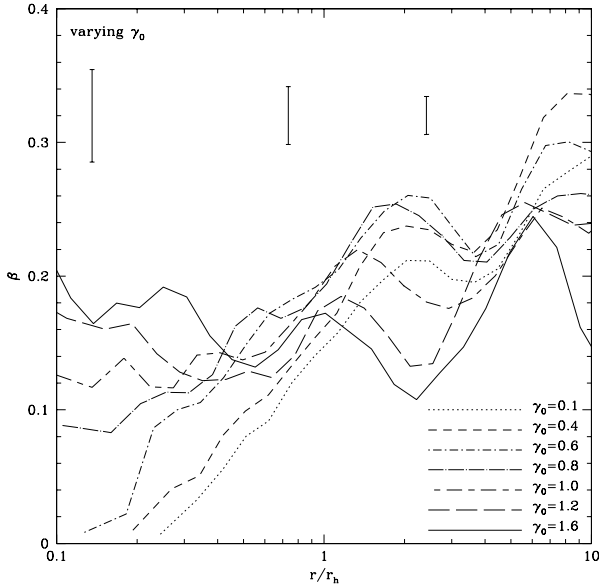


Figure 8. β as a function of radius for the simulations of suite 4. Error bars shown are typical. Simulation results shown are for haloes with density cusps of strengths as indicated.

by

$$\begin{aligned}
 (\Delta\beta)^2 = & \\
 \left(\frac{\partial\beta}{\partial\sigma_\theta^2} \right)^2 (\Delta\sigma_\theta^2)^2 + \left(\frac{\partial\beta}{\partial\sigma_\phi^2} \right)^2 (\Delta\sigma_\phi^2)^2 + \left(\frac{\partial\beta}{\partial\sigma_r^2} \right)^2 (\Delta\sigma_r^2)^2, & (10)
 \end{aligned}$$

The remarkable aspect of the observed β profiles of the remnant haloes is its near independence from the parameters varied in suites 1–3 (Figure 7, top to bottom). In all cases examined $\beta \approx 0.1$ at small r , and increases to $\beta \sim 0.2 – 0.3$ at $r \sim 10r_h$. This shows that while the remnant halo has a clear “memory” of the density profiles of the initial haloes, it has little memory of the velocity distribution of the initial haloes. There is some difference observable between the $\beta = 0.35$ and $\beta = -0.4$ cases, perhaps most noticeable in the range $0.5r_h < r < r_h$, but it is vastly smaller than the difference in the initial halo conditions.

One would also naively expect the impact parameter of the merger to have a significant effect, but it does not show any greater effect on the β profile than the orientation of the galaxies does. The independence from disc orientation is unsurprising at large radii, but also continues to small radii, where one might have expected the disc orientation to play a role.

The β profiles from the simulations of suite 4 are shown in Figure 8. As $r \rightarrow 0$, the value of β tends to 0 for the less strongly cusped initial conditions ($\gamma_0 = 0.1 – 0.6$). As the cusp strength increases, the radial anisotropy of the inner parts of the halo increases. At larger radii the anisotropy tends towards $\beta \sim 0.2 – 0.3$ for all cusp strengths, with the less strongly cusped haloes tending to have higher anisotropy.

Almost all of the β profiles share a similar non-monotonic shape. β increases at small r , reaching a peak

at $r \sim 1 – 1.5r_h$, then falls off, reaching a local minimum at $r \sim 2 – 3r_h$, before rising again. This apparent oscillatory variation of β is not associated with any tidal arms, shells, or any other observed features of the particle distribution; it is also not seen to disappear or vary to any great extent with time. A similar β profile can be seen in Figure 11 of Boylan-Kolchin & Ma (2004). Further work is required to determine its cause and importance.

Hansen & Moore (2006) argued for a universal relationship between local density slope γ and velocity anisotropy β , given in Equation 3, which we plot in each of the graphs in Figure 9. The data fit the suggested relationship for $\gamma \lesssim 2$, but do not fit for $\gamma \gtrsim 2$, where β is systematically lower than the fitting function. While it is the outer parts of the halo which have $\gamma \gtrsim 2$, and the dynamical time is longer here than in the inner parts of the halo, this is not simply because the outer halo has yet to reach an equilibrium. Simulations which ran for twice as long (until $t = 2000 \cong 28$ Gyr scaled to the Milky Way) showed identical results. The $\beta = 0.35$ initial conditions produce remnants which are a close fit to the suggested relationship, but the $\beta = -0.4$ initial conditions produce remnants which have systematically slightly lower values of β for the same γ . The fitting formula equation 3, with the smaller value for the free parameter $\xi \simeq 1.05$ (plotted as a dotted line in figure 9) does appear to provide an upper limit for β .

We observe that the haloes’ net rotation is very small; we compare to the velocity dispersion and find that $v_{rot}/\sigma < 0.1$ in the inner regions in all cases. There is slightly more rotation at large radii, but still $v_{rot}/\sigma < 0.2$ in all cases. Bulk rotation is also near negligible, with the axes of the bulk distribution remaining near fixed over a long period of time in all cases.

3.3 Halo Shape

We calculate the overall shape of the remnant halo through an iterative procedure based on diagonalizing the moment of inertia tensor

$$I_{i,j} = \sum_\alpha m_\alpha r_{i,\alpha} r_{j,\alpha}, \quad (11)$$

where the sum is over all particles considered, and $r_{i,\alpha}$ is the i coordinate of the α th particle. We start with a spherical window, centred at the densest point of the halo, which contains 50% of the mass of the halo, then determine and diagonalize its moment of inertia tensor. This determines the principle axes and the axis ratios of an ellipsoidal window which is scaled to contain 50% of the halo mass. This is then repeated to find new ellipsoidal windows until the results converge such that the volume of the window is conserved to within a fractional difference of 10^{-3} between iterations. From the ellipsoidal window we determine the axis lengths $a, b & c$ with $a \geq b \geq c$, and thus the intermediate (b/a) and minor (c/a) axis ratios. We can then define an ellipsoidal “radius”

$$\zeta = \sqrt{x'^2 + \frac{a^2 y'^2}{b^2} + \frac{a^2 z'^2}{c^2}}. \quad (12)$$

The question of whether an ellipsoidal body is prolate, oblate or triaxial can be quantified through the parameter

$$T = (a^2 - b^2)/(a^2 - c^2). \quad (13)$$

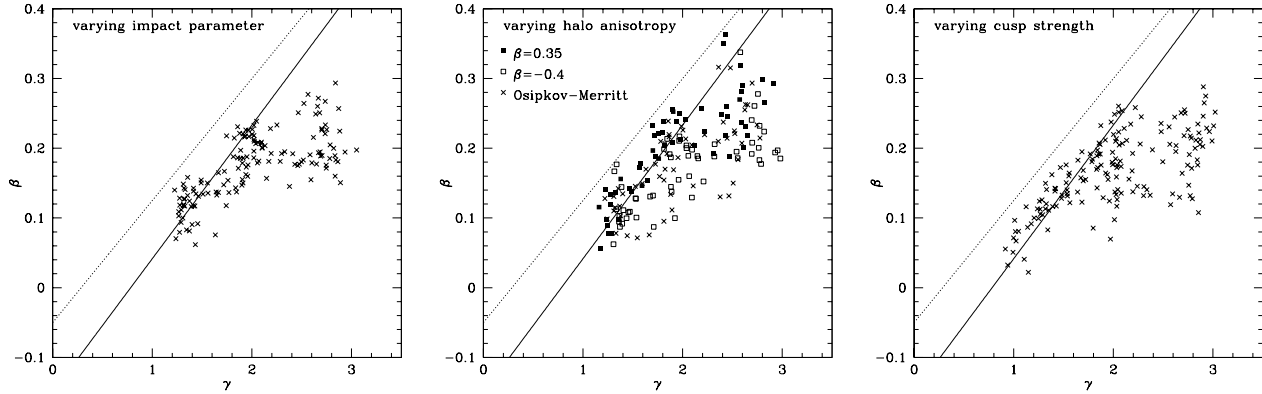


Figure 9. Anisotropy parameter β plotted as a function of the local density slope γ for mergers from suite 2 (left), suite 3 (centre), and suite 4 (right). β and γ are determined for each simulation at many points with the radial range $0.1r_h < r < 10r_h$. The lines drawn in each plot correspond to equation 3, with $\xi = 1.15$ (solid line) and $\xi = 1.05$ (dotted). In the central plot, filled squares correspond to mergers with $\beta = 0.35$ initial conditions, open squares are from the $\beta = -0.4$ initial conditions, and crosses for the Osipkov-Merritt halo initial conditions.

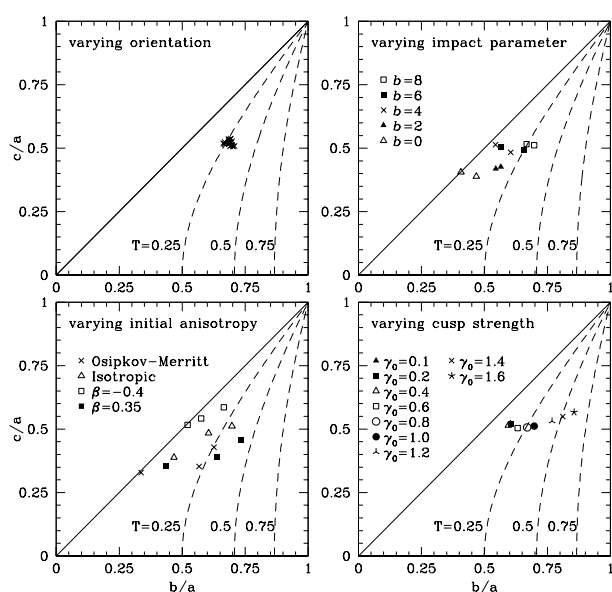


Figure 10. Minor (c/a) and intermediate (b/a) axis ratios for the simulations of all suites of simulations (as labelled). In all figures the solid diagonal indicates the position on the plot of a completely prolate halo. The dashed lines are of constant triaxiality, as indicated. For suites 2 (top-right), 3 (bottom-left) and 4 (bottom-right) the different symbols represent different simulation parameters as labelled. The three points for each initial anisotropy (suite 3) correspond to simulations with impact parameters $d = 0, 3, 8$ with, in each case, $b/a_{d=0} < b/a_{d=3} < b/a_{d=8}$.

We use this method to enable a like-for-like comparison with the simulations of Novak et al. (2006), though starting with a spherical window can cause bias.

3.3.1 Trends in halo shapes

The graphs of Figure 10, which show the ratios c/a and b/a (determined as described above) for simulations from all of our suites, tell us the following things:

- (i) Remnant haloes are significantly non-spherical ($c/a \lesssim 0.55$ in all cases shown). They are generally prolate, or at least tending towards prolate, in our simulations.
- (ii) The triaxiality of the halo at this scale ($\zeta \sim 10r_h$ for outermost particles) is barely affected by the initial inclination of the disc.
- (iii) More radial mergers (i.e. mergers with lower values of d) tend to have more prolate remnant haloes. This is true whether or not the initial haloes are isotropic.
- (iv) Tangential anisotropy in the initial halo tends to produce haloes that are more prolate, and have a higher value of c/a than in the isotropic case. Conversely, radial anisotropy in the initial halo tends to produce haloes that are more triaxial, and have a lower value of c/a than in the isotropic case.
- (v) In the range $0.4 < \gamma_0 < 1.6$, an increasing cusp strength tends to produce remnants with a greater value of b/a . This is not simply due to the decreasing size of the window containing 50% of the mass in haloes with increasing cusp strength, and is also seen if the volume of the window is defined such that it is the same for all cusp strengths.

Like Novak et al. (2006) we find that the minor axis of the stellar remnant and the major axis of the remnant halo are nearly always close to perpendicular. The major axis of the halo is always close to the plane of galaxies' original mutual orbit, and the minor axis of the stellar component is nearly always close to being perpendicular to that plane.

3.3.2 Ellipticity profiles

We wish to examine the effect of the orientation of the disc components upon the ellipticity of the remnant halo as a function of radius. In an effort to do this, we find the density at each particle by a “nearest neighbours” analysis (Casertano & Hut 1985), divide the particles into shells by

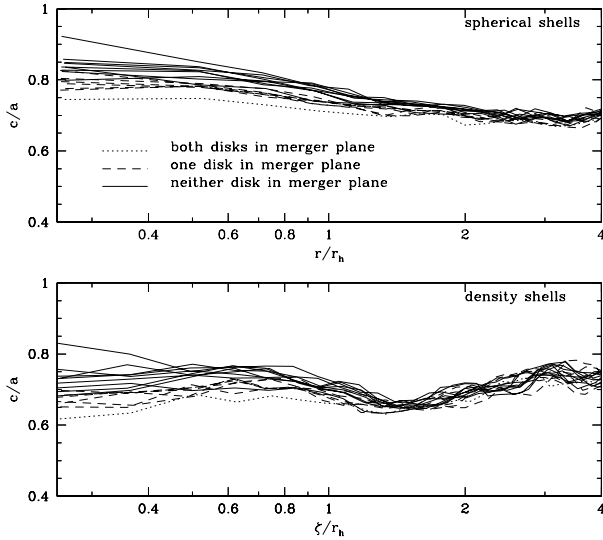


Figure 11. Minor axis ratios as a function of radius r (upper) or ellipsoidal radius ζ (lower) for the simulations of suite 1. The dotted lines corresponds to the simulation in which galaxy discs are both oriented in the merger plane, the dashed lines correspond to the simulations in which one of the discs was oriented in the merger plane.

density, and determine the axis ratios and median ellipsoidal radius of each shell. The axis ratio of the particles in a shell is found from their moment of inertia tensor (Equation 11). For comparison to Kazantzidis et al. (2004) we also divide the merger remnant halo into spherical shells, and find the axis ratio of the particles in those shells. We defined the radius of the spherical shells as being the median radius of the particles in it. The two approaches produced qualitatively similar results, though, as Athanassoula (2006) shows, using a spherical window introduces a bias towards larger values for c/a and b/a . In Figure 11 we plot the results from the both analyses.

Considered in terms of c/a at the innermost point determined, the flattest merger remnant comes from the co-planar merger, and the next four flattest remnants are from mergers with one of the discs in the orbital plane. The difference in minor axial ratio is relatively small. Using the density shells values, at the innermost point for the co-planar merger remnant c/a is ~ 0.62 , for mergers with one galaxy disc in the orbital plane it's ~ 0.67 , and for mergers with neither disc in the orbital plane it's ~ 0.72 . The simulation with orientation 16 (see Table 1) produces a notably more spherical remnant than all the other simulations ($c/a \sim 0.83$). Beyond $r \sim 1.5r_h$ the difference in c/a is negligible. There is no trend apparent in the intermediate axis ratio, b/a . These trends are exactly as one would expect.

It is reasonable to ask whether the fact that these haloes are so far from spherical invalidates the approach in Section 3.1, of using a spherically averaged density profile. In an effort to investigate this, we created density profiles based upon the density shells, found through the method described above. These profiles, while suffering somewhat from in-

creased noise, showed the same behaviour as that described in Section 3.1. This indicates that the use of spherically averaged profiles is sufficient and appropriate for the analysis of the haloes of merger remnants.

4 DISCUSSION

We have performed a number of suites of simulations, covering a number of different merger parameters. Across all these simulations we have seen that the halo cusp strength is extremely robust against changes caused by major mergers, even when there is a centrally concentrated stellar component. This is in keeping with previous results from halo only simulations (e.g. Kazantzidis et al. 2006); simulations with disc components, but initialised using a Maxwellian approximation (e.g. Aceves & Velázquez 2006) and analytical arguments (Dehnen 2005). Thus mergers, at least of gas-less equal mass galaxies, can not solve the persistent discrepancy between observations of nearby galaxies, which imply that galactic dark matter haloes have a density profile with a flat core, and the cosmological standard model, which predicts that haloes should have a cusp.

In contrast to the density profile, the velocity anisotropy of the halo has very little ‘memory’ of the initial conditions of the merger. In all cases examined, the velocity anisotropy of the remnant followed the relationship (Equation 3) suggested by Hansen & Moore (2006) relatively closely for $\gamma \lesssim 2$, but β was systematically lower than predicted for $\gamma \gtrsim 2$. That these results are nearly independent of initial anisotropy is very encouraging. The overwhelming majority of merger simulations to date have been performed with isotropic haloes, while the haloes found in cosmological simulations are typically radially anisotropic. A strong dependence on anisotropy would suggest that the approximation of isotropy in the halo was a poor one, which would have cast doubt upon results from simulations using it. The velocity anisotropy of the halo is clearly a less robust property than its density profile.

Given the shape of the dark matter haloes observed by, for example Buote et al. (2002), the results of Section 3.3 are of particular importance. Axis ratios c/a in the range 0.37 ± 0.04 (as seen for NGC720) are seen for all initial halo anisotropies except $\beta = -0.4$, in cases with sufficiently small impact parameters. Simulations which incorporate the effects of gas physics (e.g. Novak et al. 2006) find remnant haloes which are significantly more spherical. It is likely, therefore, that galaxies with such highly flattened haloes were formed from near-radial trajectory, very gas-poor mergers in which collisionless dynamics dominate.

That the remnant halo is closest to completely prolate for mergers with low impact parameters is unsurprising, and was recognised in the literature as far back as 1983 Villumsen in the case of completely spherical initial models. In the $d = 0$ case, the major axis of the remnant is in the same direction as the initial motion of the galaxy centres.

The dependence of remnant shape on initial anisotropy of the haloes is far less trivially understandable, but is likely to be related to the radial-orbit instability (e.g. Barnes 1985; Dejonghe & Merritt 1988). Spherical systems with large numbers of radial orbits are known to be unstable to deformation towards a barred or triaxial shape. The radial-

orbit instability is also known to reduce the central concentration of models (e.g. Merritt & Aguilar 1985), which could explain the slight decrease in cusp strength seen in the $\beta = 0.35$ model remnants (Figure 6).

It is known that a steep cusp in a triaxial model causes orbit-scattering which can have a significant effect on its shape (Valluri & Merritt 1998), reducing the triaxiality. The effect of increasing the cusp strength of our haloes is to make the remnants more spherical (less prolate, i.e. increasing b/a), but this means that the most strongly cusped haloes are *more* triaxial than the least strongly cusped ones.

Increasing the cusp strength of the halo puts more of the mass of the halo at radii smaller than the impact parameter of the merger. This is similar to the effect of increasing the impact parameter of the merger, which we have shown increases b/a for the remnant. It is likely that this explains the trend in remnant shape with cusp strength.

ACKNOWLEDGEMENTS

PJM acknowledges the support of an EU Marie Curie Fellowship, and of the UK Particle Physics and Astronomy Research Council (PPARC) through a research student fellowship. Astrophysics research at the University of Leicester is also supported through a PPARC rolling grant.

REFERENCES

Aceves H., Velázquez H., 2006, Revista Mexicana de Astronomía y Astrofísica, 42, 41

Allgood B., Flores R. A., Primack J. R., Kravtsov A. V., Wechsler R. H., Faltenbacher A., Bullock J. S., 2006, MNRAS, 367, 1781

Athanassoula E., 2004, in IAU Symposium, Ryder S., Pisano D., Walker M., Freeman K., eds., pp. 255+—, 2006, MNRAS, submitted

Barnes J., 1985, in IAU Symp. 113: Dynamics of Star Clusters, Goodman J., Hut P., eds., pp. 297–299

Barnes J. E., 1988, ApJ, 331, 699

Boylan-Kolchin M., Ma C.-P., 2004, MNRAS, 349, 1117

Buote D. A., Canizares C. R., 1996, ApJ, 457, 177—, 1998, MNRAS, 298, 811

Buote D. A., Jeltema T. E., Canizares C. R., Garmire G. P., 2002, ApJ, 577, 183

Casertano S., Hut P., 1985, ApJ, 298, 80

Cuddeford P., 1991, MNRAS, 253, 414

Dehnen W., 1999, AJ, 118, 1201—, 2000, ApJ, 536, L39—, 2002, Journal of Computational Physics, 179, 27—, 2005, MNRAS, 360, 892

Dehnen W., McLaughlin D. E., 2005, MNRAS, 363, 1057

Dejonghe H., Merritt D., 1988, ApJ, 328, 93

Dubinski J., Carlberg R. G., 1991, ApJ, 378, 496

Hansen S. H., Egli D., Hollenstein L., Salzmann C., 2005, New Astronomy, 10, 379

Hansen S. H., Moore B., 2006, New Astronomy, 11, 333

Hernquist L., 1990, ApJ, 356, 359—, 1993, ApJS, 86, 389

Hernquist L., Ostriker J. P., 1992, ApJ, 386, 375

Ibata R., Lewis G. F., Irwin M., Totten E., Quinn T., 2001, ApJ, 551, 294

Katz N., Gunn J. E., 1991, ApJ, 377, 365

Kazantzidis S., Kravtsov A. V., Zentner A. R., Allgood B., Nagai D., Moore B., 2004, ApJL, 611, L73

Kazantzidis S., Zentner A. R., Kravtsov A. V., 2006, ApJ, 641, 647

Klypin A., Zhao H., Somerville R. S., 2002, ApJ, 573, 597

Majewski S. R., Skrutskie M. F., Weinberg M. D., Ostheimer J. C., 2003, ApJ, 599, 1082

McMillan P. J., 2006, Ph.D. Thesis

McMillan P. J., Dehnen W., 2007, MNRAS, submitted

Merritt D., 1985, MNRAS, 214, 25P

Merritt D., Aguilar L. A., 1985, MNRAS, 217, 787

Moore B., Governato F., Quinn T., Stadel J., Lake G., 1998, ApJL, 499, L5

Naab T., Burkert A., 2003, ApJ, 597, 893

Naab T., Jesseit R., Burkert A., 2006, MNRAS, 372, 839

Navarro J. F., Frenk C. S., White S. D. M., 1996, ApJ, 462, 563

Negroponte J., White S. D. M., 1983, MNRAS, 205, 1009

Novak G. S., Cox T. J., Primack J. R., Jonsson P., Dekel A., 2006, ApJL, 646, L9

Osipkov L. P., 1979, Pis ma Astronomicheskii Zhurnal, 5, 77

Power C., Navarro J. F., Jenkins A., Frenk C. S., White S. D. M., Springel V., Stadel J., Quinn T., 2003, MNRAS, 338, 14

Taylor J. E., Navarro J. F., 2001, ApJ, 563, 483

Toomre A., 1964, ApJ, 139, 1217

Toomre A., Toomre J., 1972, ApJ, 178, 623

Valluri M., Merritt D., 1998, ApJ, 506, 686

Villumsen J. V., 1983, MNRAS, 204, 219

White S. D. M., 1978, MNRAS, 184, 185

Widrow L. M., Dubinski J., 2005, ApJ, 631, 838